Review article

Open Access

Ren-Jye Shiue, Dmitri K. Efetov, Gabriele Grosso, Cheng Peng, Kin Chung Fong
and Dirk Englund*

Active 2D materials for on-chip nanophotonics and quantum optics

Abstract: Two-dimensional materials have emerged as promising candidates to augment existing optical networks for metrology, sensing, and telecommunication, both in the classical and quantum mechanical regimes. Here, we review the development of several on-chip photonic components ranging from electro-optic modulators, photodetectors, bolometers, and light sources that are essential building blocks for a fully integrated nanophotonic and quantum photonic circuit.

Keywords: optoelectronics; quantum information processing; 2D materials; nanophotonics; bolometer; single photon source; photonic integrated circuit.

1 Introduction

Photonic integrated circuits (PICs) allow compact optoelectronic component integration with high stability and low optical losses [1–3]. These properties make them appealing to both classical and quantum information processing applications. However, many applications demand device properties that require multiple disparate materials. For example, light sources must have a larger band gap than photodetectors. Optical modulators rely on materials with a strong electro-optic (E-O) effect [4], and still other materials may be required for non-linear optical functions or non-classical light sources.

Traditionally, the way to approach the problem of integrating multiple materials would require heterogeneous material growth or wafer-bonding approaches. However, these approaches can be extremely complex and challenging. For instance, the integration of two types of semiconductors – wafer bonding of silicon and III/V InP gain layers – is a major engineering challenge [5]. Two-dimensional (2D) materials, on the other hand, can greatly simplify the assembly of active optoelectronic systems on-chip. They can be conformally layered with relative ease and are "glued" sufficiently strongly by van der Waals (vdW) forces. The advent of such vdW material platforms has proven extremely rich and fruitful for not only electronic [6] but also photonic devices and systems [7]. The primary applications of vdW materials integrated into PICs are in optical interconnects and quantum information processing. Here, we review recent progress in these efforts, focusing on graphene-based E-O modulators and photodetectors, and light sources (classical and quantum) based on 2D transition metal dichalcogenides (TMDCs) and hexagonal boron nitride (hBN). For brevity, we will focus on many areas of our work, but seek to reference other works in the broader context of a wide and rapidly growing research field of 2D vdW materials for quantum optics and optoelectronics. Table 1 summarizes the list of devices that emerge for different nanophotonic and quantum photonic applications with different 2D materials (heterostructures).

2 Heterogeneous integration of 2D materials with nanophotonic devices

Nanophotonic devices, including waveguides and cavities, can control optical fields at subwavelength dimensions. Coupling a nanophotonic cavity to a 2D material can enhance light-matter interaction to enable spectrally selective and orders-of-magnitude increased optical absorption and fluorescence. Coupling to nanophotonic waveguides

*Corresponding author: Dirk Englund, Department of Electrical Engineering and Computer Science, Massachusetts Institute of Technology, Cambridge, MA 02139, USA, e-mail: englund@mit.edu
Ren-Jye Shiue, Dmitri K. Efetov, Gabriele Grosso and Cheng Peng:
Department of Electrical Engineering and Computer Science, Massachusetts Institute of Technology, Cambridge, MA 02139, USA
Kin Chung Fong: Raytheon BBN Technologies, Quantum Information Processing Group, Cambridge, MA 02138, USA

Table 1: List of applications of active nanophotonic and quantum photonic devices based on 2D materials.

Applications	Materials	Band gap	Photonics integration	Operation mechanism
E-O modulators	Graphene	Zero gap	Waveguides [8, 9]	Electro-absorption
	Graphene/hBN heterostructures	Zero gap	PPC cavities [10]	Electro-absorption
	Graphene	Zero gap	Ring resonators [11–13]	Electro-absorption
Photodetectors	Graphene/hBN heterostructures	Zero gap	Waveguides [14–16]	Photovoltaic and photothermoelectric effects
	BP	0.3–2 eV	Waveguides [17]	Photovoltaic and bolometric effects
(Classical) light emitters/lasers	MoS_2	~ 2 eV	GaP PPC [18] cavities	Purcell enhancement
	WSe_2, WS_2	1.5–2.5 eV	PPC cavities/micro-disk resonators [19, 20]	Purcell enhancement/lasing
Bolometers/single photon detectors	Graphene/hBN heterostructures	Zero gap	PPC cavities	Johnson noise thermometry [21]
Single photon emitters	hBN	~ 6 eV	N/A	Atomic defects [22]
	TMDCs	1.5–2.5 eV	N/A	Atomic defects [23, 24]

provides broadband enhancement. In this section, we discuss theory and experiments of heterogeneously integrated 2D materials with optical cavities and waveguides.

2.1 Absorption enhancement in cavity-integrated 2D materials

Using a temporal coupled mode theory (CMT) that considers the absorption of 2D materials coupling to an optical cavity [25], Gan et al. showed that the reflection, transmission, and absorption of a cavity strongly depend on two fundamental parameters: the intrinsic cavity loss rate κ_c without 2D materials and the excess loss rate introduced by the absorption of 2D materials κ_{2D} in the cavity. There are two important regimes for such a coupled 2D materials-cavity system: strong attenuation of either the cavity reflection or transmission with large κ_{2D}/κ_c ratio and, on the contrary, maximum absorption in 2D materials with a critical coupling condition, i.e. $\kappa_{2D} = \kappa_c$.

We now discuss an experimental example of the enhanced absorption in graphene integrated with a planar photonic crystal (PPC) cavity. Figure 1A shows the finite-difference time-domain (FDTD) simulation of the cavity field of a PPC cavity fabricated by drilling periodic holes on a suspended gallium phosphide (GaP) membrane (180 nm). The PPC has a lattice constant a of 420 nm with an air-hole radius of 0.29a. A linear three-missing-hole (L3) defect in the middle of the PPC lattice serves to form confined resonant modes. Figure 1B shows the reflection spectrum of the cavity under the illumination of a broadband (super-continuum laser) source via a cross-polarization confocal microscope. The blue spectrum corresponds to the cavity without graphene deposition, showing a

single sharp resonant peak. The graphene was prepared by mechanical exfoliation and then transferred on top of the cavity [27], as shown in the optical image in Figure 1B. The coupling of the graphene sheet to the evanescent field of the cavity results in reduction of the cavity Q from 2640 to 360, while the resonance red-shifts by 1.8 nm, indicated by the red spectrum acquired after graphene deposition. The cavity reflection dropped by 20 dB at 1477.3 nm (the resonance wavelength of the unloaded cavity). Thus, the naturally weak absorption (2.3%) of graphene [28] from normal incidence is dramatically amplified by coupling to the nanocavity.

From CMT, we deduced the decay rates of κ_c and κ_{cg} to be $1.9 \times 10^{-4}\ \omega_0$ and $2.4 \times 10^{-2}\ \omega_0$, respectively [25], indicating that graphene loss accounts for approximately 92% of the total loss inside the nanocavity. By correlating the optical conductivity of graphene to the cavity loss and cavity field distribution, we extracted the single-layer graphene (SLG) complex dielectric function on top of the cavity to be $\sigma_{g//} = 4.64 + 4.62i$ and $\sigma_{g\perp} = 2.79$ at a wavelength of 1477 nm, in good agreement with other reported values [29].

2.2 Fluorescence enhancement of 2D materials in an optical cavity

Because the local density of optical states is enhanced in a nanocavity, the spontaneous emission (SE) rate of fluorescent materials is also increased, due to the Purcell effect. This Purcell enhancement has been used to greatly improve the SE internal quantum efficiency of 2D materials [18, 30]. Here, we review both experimental results and quantitative analyses of the SE rates of 2D materials coupled to PPC cavities similar to those in the previous
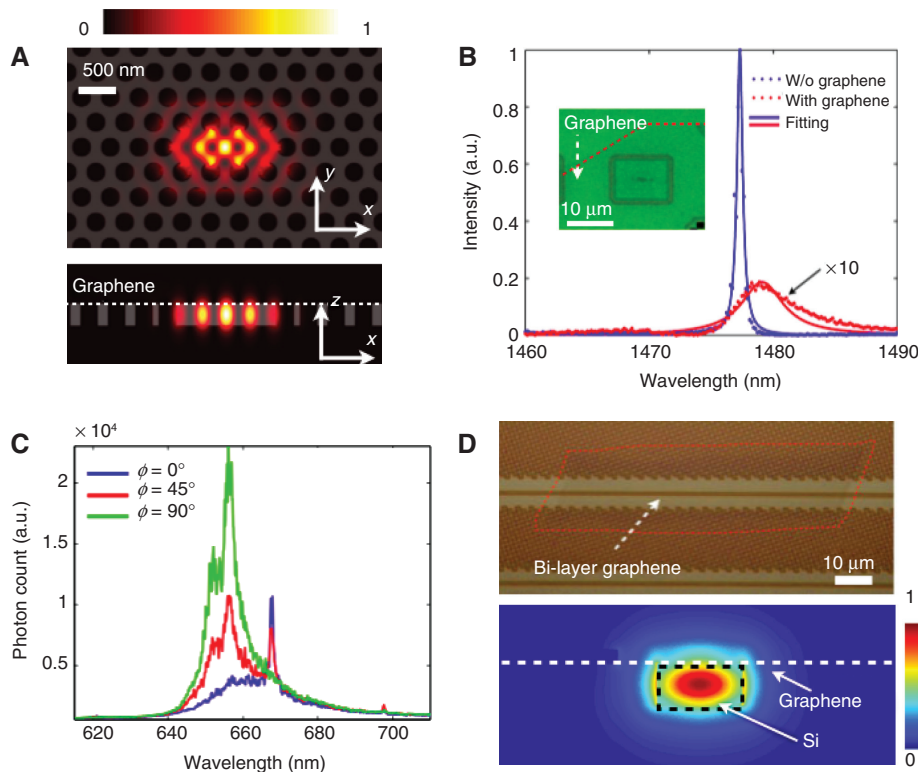
Figure 1: (A) Simulated electric field distribution of a PPC L3 cavity. Bottom panel shows the cross-sectional view of the cavity mode. The graphene layer on the surface of the suspended PPC membrane can couple to the evanescent field of the resonant mode. (B) Reflection spectrum of a GaP PPC cavity before and after coupling to a single layer of graphene. Inset: Optical image of the graphene-PPC cavity device. (C) Fluorescence of single-layer MoS_2 coupled to a PPC cavity [18]. Red, blue, and green curves show the PL collect at a polarization angle of 0°, 45°, and 90°. (D) Top: Optical image of a 70-μm-long graphene couples to a silicon waveguide. Bottom: Simulated waveguide mode couples to the graphene sheet deposited on the top surface of silicon [26].

section. These cavities, which are also based on GaP membranes, have resonant modes in the wavelength range of 600–700 nm, overlapping with the fluorescence of molybdenum disulfide (MoS_2), a direct band-gap 2D semiconductor belonging to the group of TMDCs [31, 32].

We measure the fluorescence of the cavity-MoS_2 system on a micro-photoluminescence (PL) confocal microscope with a 532-nm continuous-wave excitation laser, focused to a beam diameter of 400 nm with a power of 50 μW. Figure 1C shows the PL collected from the L3 defect, exhibiting several narrow peaks with enhanced PL intensity compared with MoS_2 deposited on a GaP substrate without the cavity. The PL exhibits strong polarization dependence, which is resolved by collecting the PL at a polarization angle ϕ with respect to the cavity along y-axis. Blue, red, and green curves show the PL at $\phi = 0°$, 45°, and 90°, respectively. The two peaks of the MoS_2-cavity PL agree to the expected resonant wavelengths, and the polarization dependence of the peaks corresponds well to that of the L3 cavity given by 3D FDTD simulations [33, 34]. The SE rate of the MoS_2 in the cavity is proportional to

the Purcell factor, which is a function of the cavity Q and the effective mode volume V_{mode}. In this particular sample, we deduced Purcell factors ranging from 20 to 80 with a cavity $Q \sim 300$, yielding a maximum seven-fold enhancement in the PL intensity.

For other heterogeneous TMDC material systems, Wu et al. integrated WSe_2 with PPC cavity ($Q \sim 8000$), showing enhanced Purcell factor of $F \sim 600$ [19]. Ye et al. coupled WS_2 to the whispering gallery mode of a Si_3N_4/HSQ microdisk resonator [20], and Salehzadeh et al. implemented MoS_2 with SiO_2 disk resonators [35]. In the above studies, strongly enhanced PL in 2D TMDCs resulted in reduced lasing thresholds, promising low-threshold on-chip light sources in 2D materials-based heterostructures. When the coupling rate of the 2D materials to the cavity field becomes even higher, the cavity-2D material coupling enters the strong coupling regime, where the energy of cavity polariton mode splits and the exciton dipoles undergo Rabi oscillations. Liu et al. observed MoS_2 strongly coupled to a distributed Bragg reflector microcavity [36], showing a Rabi splitting energy of ~ 50 meV.

2.3 Absorption enhancement of 2D materials integrated with optical waveguides

Thus far, we have described the enhancement of the light-matter interaction via optical resonators. This effect is inherently narrowband due to the narrow resonant bandwidth of the resonators. Coupling 2D materials with a nanophotonic waveguide can enhance the light-matter interaction non-resonantly and hence span a broader bandwidth [16]. The top panel of Figure 1D provides an example device consisting of a bilayer graphene flake deposited across ~ 70 μm over a 520-nm-wide silicon-on-oxide (SOI) waveguide, fabricated from an SOI wafer with a 220-nm-thick Si membrane using the standard shallow trench isolation module. To prevent the graphene from fracturing at the edges of the waveguide, the chip was planarized by backfilling with a thick SiO_2 layer and polishing the surface with a chemical-mechanical polishing step to reach the top Si layer.

The quasi TE-mode field simulation in the bottom panel of Figure 1D shows the evanescent field overlap to the graphene. From the complex effective index of graphene, we can estimate an absorption coefficient of 0.085 dB/μm. Experimentally, we observed that a 70-μm-long graphene bilayer causes a transmission loss around 6.2 dB over the wavelength range from 1510 to 1580 nm. The transmission loss deduced from the simulation results [16] is ~ 5.95 dB, and we attribute the measured excess loss to the interface scattering between graphene and the waveguide surface.

The absorption coefficient could be greatly increased (to ~ 0.2 dB/μm) by a stronger evanescent field of the waveguides that support a transverse magnetic guide mode [8, 37] or by thinner waveguides. Other strategies to enhance the absorption include sandwiching the graphene layer inside a dielectric slot waveguide [38] or modifying the electric field distribution by creating an air slot in the middle of a channel waveguide. Wang et al. achieved absorption as high as ~ 1 dB/μm by coupling graphene to such a silicon air-slot waveguide [39].

3 Active optoelectronics based on PIC-integrated vdW heterostructures

In the following sections, we discuss 2D materials-based E-O modulators and photodetectors integrated with nanophotonic cavities and waveguides.

3.1 Graphene-cavity high-speed E-O modulators

Graphene modulators rely on the Pauli blocking effect [40, 41], which is illustrated in Figure 2A. Electrostatic gating raises (lowers) the Fermi level E_F of graphene, causing reduction in graphene's optical absorption for photon frequencies $\hbar\omega < 2 |E_F - E_{CNP}|$, where $E_F - E_{CNP}$ is the difference in the electron Fermi energy from the charge neutrality point (CNP). Using the Pauli blocking effect in a 50-μm-long SLG coupled to a SOI waveguide [8], Liu et al. demonstrated broadband modulation for wavelengths from 1.35 to 1.6 μm with 3 dB modulation depth. Recently, improved device designs using mutually gated SLG capacitor structures on waveguides achieved modulation depths of 6 dB [9] and 16 dB [42].

Resonators can shrink the size of such graphene modulators. For instance, we demonstrated a graphene modulator based on an air-slot cavity with wavelength-scale mode volume that achieved > 10 dB modulation depth in the telecommunication band [43]. The graphene was gated using an electrolyte layer [poly(ethylene oxide) (PEO) plus $LiClO_4$], requiring a relatively small swing voltage of 1.5 V for a modulation contrast of 10 dB.

The relative low speed of electrolyte gating, with a cutoff frequency response < 1 MHz [44], prompted us to develop a high-speed device based on a graphene capacitor on the photonic crystal cavity [10], as illustrated in Figure 2B. The capacitor consisted of a boron nitride (BN)/graphene/BN/graphene/BN five-layer stack that was produced by the vdW assembly technique and transferred onto a quartz substrate [45], with lower parasitic capacitance compared to more commonly used SiO_2/Si substrates. The silicon-membrane-based air-slot PPC cavity was then transferred and aligned with this graphene capacitor, producing the device shown in Figure 2B.

Figure 2C shows the normalized cavity reflection at $\lambda = 1551$ nm as a function of V_G, indicating a modulation depth of 3.2 dB. The modulation for negative bias voltage, -5.6 V $< V_G < 0$ V, mimicked that for positive voltage, as the doping types of the top and bottom graphene layers were reversed. The cavity reflectivity is symmetric about the CNP at $V_G = 0.2$ V.

The measured E-O S_{21} parameter, shown in Figure 2D, indicates a 3 dB cutoff frequency of 1.2 GHz, corresponding to the resistance-capacitance (RC)-limited time constant of the dual-layer graphene capacitor. A CMT model similar to that described in Section 2.1 indicates that the real optical conductivity of graphene, σ_{gr}, at the maximum gate voltage is reduced only to half of the ungated value
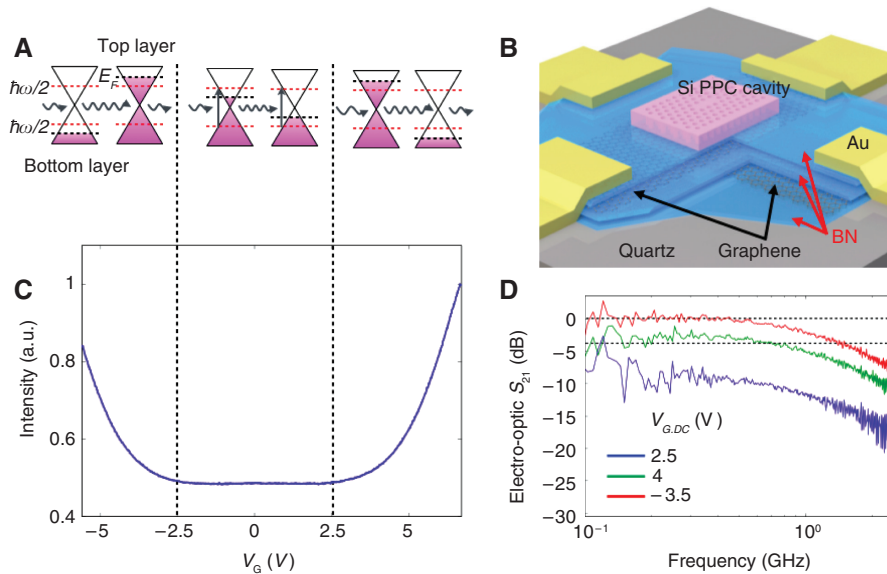
Figure 2: (A) Schematic of the electro-absorptive effects in a capacitor structure consisting of two graphene layers ("top" and "bottom") separated by hBN. When the Fermi level in graphene rises (drops), the absorption of graphene reduces due to the Pauli blocking of the interband transition of the electrons in graphene. (B) Schematic of the high-speed graphene E-O modulator [10]. (C) Normalized reflection intensity as a function of the gate voltage (V_G). (D) Normalized E-O S21 of the graphene E-O modulator as a function of frequency.

(at the graphene CNP). Thus, a higher contrast would be possible at higher gate voltage, but would push the device dangerously close to breakdown ($V_{breakdown} = 0.3–0.8$ V/nm [46, 47]) across the 10-nm-thick BN dielectric layer of the graphene capacitor. Higher contrast could be achieved at longer operation wavelengths, or with the use of high-k materials or chemical doping of the graphene layers near the Pauli blocking regime.

The graphene capacitor in Figure 2 has an area of ~ 100 μm^2, a capacitance of 320 fF, and a corresponding switching energy $CV^2/2 \sim 1$ pJ/bit. Because the graphene parallel-plate capacitor was much larger than necessary as the area of the optical mode is only ~ 0.5 μm^2, limiting the area of the graphene capacitor to the optical mode (~ 200 times smaller) would lead to a reduction of two orders of magnitude in the switching energy and RC time constant. As the cavity optical bandwidth is large (~ 600 GHz for a Q value of 300), such graphene-PPC modulators could enable high modulation contrast, exceptionally low energy consumption, and a much broader modulation bandwidth than Si modulators based on free-carrier dispersion [48–50].

Several other very promising graphene modulator designs have been introduced. Silicon ring resonators [11, 12] with graphene-based modulation showed a 12.5 dB modulation depth, and a graphene-silicon nitride ring resonator enabled a high modulation contrast of 15 dB per 10 V driving with ~ 30-GHz operation speed [13]. Finally, silicon Mach-Zehnder interferometers have also been

integrated with graphene, producing a modulation depth of > 4 dB and cutoff of 2.5 GHz [51].

3.2 Graphene-waveguide high-responsivity photodetector

Photodetectors in PICs require a different material that is absorptive where the PIC is transparent. Today, these include epitaxial Ge photodetectors [52], wafer-bonded InP [53], or Si with mid-band-gap states [54]. Graphene has recently emerged as a promising alternative that promises simple layer-transfer integration and photoresponse from ultraviolet (UV) all the way to the near-infrared, mid-infrared, and terahertz (THz) regimes. Moreover, graphene detectors can be extremely fast – early studies in graphene-based photodetectors show ultrafast photoresponse up to 40 GHz with zero bias voltage [55] – and graphene's strong electron-electron interaction allows multiple hot electron-hole pairs to be generated for each incident photon [56–58], boosting detection responsivity. Recent advances in wafer-scale growth and transfer of graphene are promising for integration of graphene with complementary metal-oxide-semiconductor (CMOS) processes or with arbitrary materials, likely using back-end-of-line processing steps.

Figure 3A sketches a waveguide-coupled graphene photodetector [15] fabricated on a CMOS-compatible PIC. A stack of 40-μm-long hexagonal BN (hBN)/SLG/hBN,
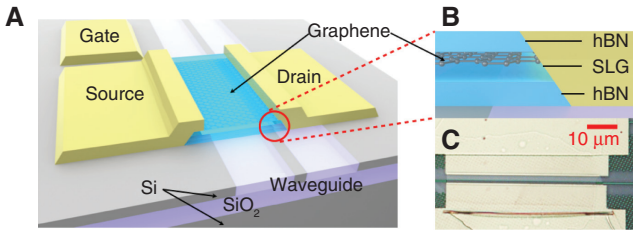
Figure 3: (A) Schematic of the graphene/boron nitride heterostructure photodetector integrated with a silicon box waveguide [15]. (B) Cross-sectional view of the side-contacted BN/SLG/BN detector. (C) Optical image of the finished waveguide-graphene photodetector.

transferred onto the PIC using vdW assembly [45], serves as the photodetector. Figure 3C shows the completed structure. The drain electrode is positioned only 200 nm from the waveguide to induce a pn junction [59, 60] near the optical mode [61].

The hBN/SLG/hBN stack decreased the waveguide transmission by 2.2 dB, corresponding to an absorption coefficient of 0.055 dB/μm, consistent with the simulated results for the waveguide evanescent field coupling to the SLG [16]. We used a polymer electrolyte (PEO and LiClO$_4$) layer covering the entire chip to independently tune the

graphene Fermi level and electric field across the waveguide mode [62–65]. Figure 4A presents responsivity measurements (defined as the ratio of the short-circuit photocurrent I_{ph} to the optical power P_{in} in the waveguide, i.e. $R = I_{ph}/P_{in}$) as a function of V_{GS} and V_{DS}, showing a six-fold pattern in the photocurrent, which qualitatively matches the behavior of the photothermoelectric effect [66, 67]. The photocurrent reaches a maximum of 0.36 A/W at $V_{GS} = 2$ V and $V_{DS} = 1.2$ V.

The high-speed intensity response of this detector was beyond the capabilities of commonly available E-O modulators. As a substitute, we interfered two detuned narrowband (1 MHz) telecom lasers to produce an intensity modulation at δf. Figure 4B plots the relative optical-to-electrical response of the detector received on an electrical spectrum analyzer (maximum frequency 50 GHz) at different δf. This measurement indicates a 3 dB cutoff frequency at 42 GHz, matching the highest reported graphene photodetector speed [14]. Sending pseudorandom on-off-keyed data produced a clear eye-opening diagram at 12 Gbit/s (inset of Figure 4B).

Waveguide-integrated graphene photodetectors are possible with CMOS-compatible processes [61]. In addition to exfoliated graphene devices, large-scale
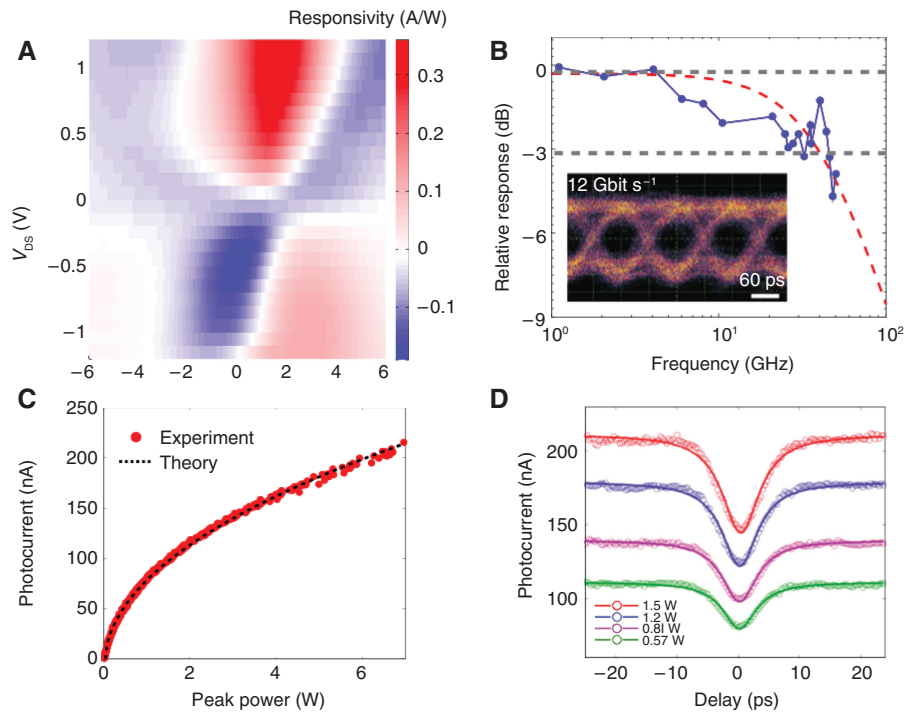

Figure 4: (A) Photo-responsivity of the graphene detector as a function of drain-source voltage (V_{DS}) and gate-source voltage (V_{GS}). (B) High-speed response of the photodetector. The red dashed line shows the fitting to the experimental results with an RC low-pass filter model. (C) Photocurrent as a function of peak power under the excitation of pulse laser. (D) Autocorrelation traces of the ultrafast graphene autocorrelator at different peak powers.

chemical vapor deposition-grown graphene integrated with waveguides can achieve a data rate of 50 Gbits/s [14], and high-responsivity by integrating with a silicon air-slot waveguide [39]. Owing to the broadband absorption of graphene, waveguide-integrated graphene heterostructure also enables photodetectors for mid-infrared wavelengths [68]. For other 2D materials, black phosphorus (BP)-based photodetectors have drawn great attention due to their small band gap that is promising for telecommunication and mid-infrared wavelength ranges [17, 69]. Heterogeneously integrated BP-silicon photodetectors have shown up to 6 A/W responsivity with > 3 GHz speed.

3.3 Ultrafast on-chip autocorrelator

The photocurrent presented in the previous section exhibits a non-linear photoresponse with a peak power that is > 50 mW. The power-dependent curve (Figure 4C) fits well by a power law of $I_{ph} \propto P_{in}^{0.47}$, suggesting supercollision-dominated cooling mechanism [70]. The picosecond-scale non-linear photocurrent is desirable for on-chip optical signal characterization, e.g. ultrafast optical sampling and autocorrelation measurements. In Figure 4D, we plot photocurrent traces as a function of the time delay Δt between pairs of 250-fs laser pulses for a range of incident powers. These traces show a clear dip at $\Delta t = 0$ with a width corresponding to the detector's carrier relaxation time of ~ 3 ps. In this device, strong non-linear photoresponse at low peak power could enable a more efficient on-chip autocorrelator compared with existing autocorrelators based on free-space parametric frequency conversion and two-photon absorption in semiconductor waveguides [71–73], while keeping a footprint of only 40 μm in length. The femtosecond thermalization of graphene's hot electrons suggests that the timing resolution of the on-chip autocorrelator is possibly down to sub-50 fs [74]. It is also important to note that this graphene-based autocorrelator supports a broad spectral range from 1500–1800 nm.

3.4 Ultrasensitive graphene-based bolometers and single photon detectors

With its exceptionally small electronic heat capacity [75–79] and weak electronic heat dissipation [64], graphene is also a promising material platform for ultrasensitive thermal detectors [80–82]. The exceedingly low number of atoms in a typical graphene device and the vanishing density of states at the CNP result in a record-low electronic specific heat, which is on the order of one Boltzmann constant. Hence, a graphene-based bolometer is comparable to some of the best nano-calorimeters [81, 83]. Additionally, the small size of the Fermi surface and the high energy of graphene's phonons result in a strongly suppressed heat flow from hot electrons into the phonon bath. With these unique thermal properties, graphene is a natural heat absorber for bolometer applications and allows for a high temperature rise by incident radiation, even down to the energy quanta of a single photon.

To investigate graphene's thermal properties and to demonstrate the proof of concept of the graphene bolometer, we investigated a Johnson noise thermometry circuit [21, 78, 84] to directly read the electronic temperature using the Johnson-Nyquist theorem. As shown in Figure 5A, the graphene device is impedance-matched with an inductor-capacitor (LC) matching network, which enables maximal transmission of the generated noise power. The signal is further amplified using a state-of-the-art low-noise amplifier, resulting in an overall temperature sensitivity that approaches 0.001 K/Hz$^{1/2}$. A directional coupler is used to apply Joule heating pulses and to simultaneously monitor the response of the electronic temperature, which enables direct measurements of the electronic cooling mechanisms through the study of the electronic thermal conductance G_{th}.

The heat transfer P is dominated by electron-phonon cooling and follows a high power law $P = \sigma A(T_e^4 - T_p^4)$, where σ is the electron-phonon coupling parameter, A is the graphene area, T_e is the electron temperature, and T_p is the phonon temperature. Figure 5B shows the typical data taken at different temperatures. Through the relation $G_{th} = P/\Delta T_e$, we can extract the thermal conductance, which we find to be on the order of 0.2 nW/K (Figure 5C). This corresponds to a noise equivalent power of the bolometer of 0.4 pW/K at 2K, as given by the product of G_{th} and the temperature sensitivity. Using a much cleaner graphene device at the CNP, the bolometer is predicted to reach an even lower NEP of ~ 10^{-21} W/Hz$^{1/2}$ [78].

The above extracted parameters make it possible to engineer a graphene-based device that could detect a single photon in the frequency range from UV to GHz. Figure 5D shows a device concept for a thermal graphene-based single photon threshold detector. High quantum efficiency can be achieved by critical coupling of the graphene to a photonic crystal cavity. The graphene sheet is further coupled to two closely spaced superconducting electrodes that form a Josephson junction and allow for a supercurrent to flow through the graphene [85–87]. Upon absorption of a single photon, the temperature of
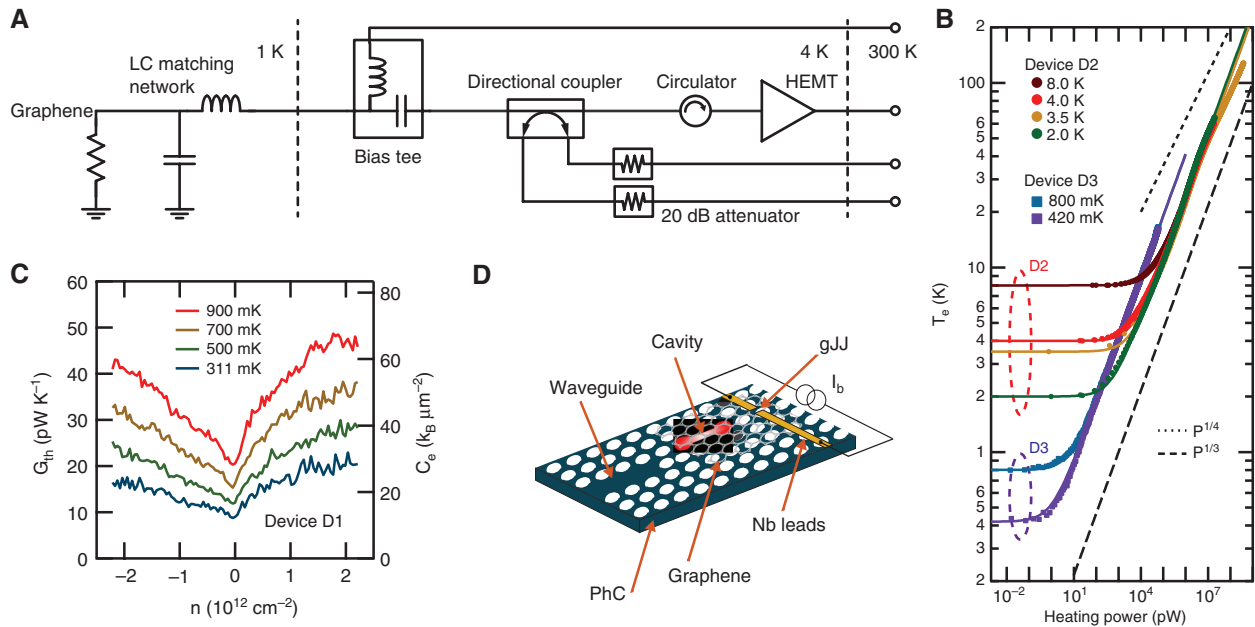
Figure 5: (A) Schematics of a graphene bolometer circuit [21, 78]. Due to its exceedingly small electronic heat capacity, the graphene sheet acts as an ultrasensitive heat absorber. The change of its electronic temperature T_e is read out by a Johnson noise thermometry scheme that provides a sensitivity in the range of mK/Hz$^{1/2}$. Here, microwave signals from the graphene are transmitted through an impedance matched LC circuit and amplified by a low noise amplifier. (B) The response of T_e to Joule heating. (C) The resulting electronic thermal conductance and the electronic specific heat due to electron-phonon cooling. (D) Schematics of a proposed graphene-based single photon detector. A graphene sheet is placed on a photonic crystal cavity for maximal quantum efficiency. The graphene is proximitized by two superconducting electrodes that allow single photon read out through the Josephson effect.

the device is increased above the critical temperature of the superconductor, creating a detectable voltage pulse across the device.

4 vdW materials for single photon generation

A single photon emitter (SPE) is a critical element for quantum information processes, including quantum networks [88] and photonic quantum computing [89]. Layered materials have recently shown quantum light emission, paving the way to new applications of this emerging class of materials. Compared with other SPEs, 2D materials have the potential to be easily integrated into complex photonic structures and enable new chip designs for quantum applications. Moreover, most are stable and can easily be gated. In this section, we review some of the recent discoveries of quantum optics applications of 2D materials in both TMDC semiconductors and insulators, and the potential high impact that this technology can bring for future efficient quantum communication devices.

4.1 Single photon source in semiconductor TMDCs

TMDCs are layered semiconductors with direct band gap at the monolayer level [31, 32]. At room temperature, PL is mainly dominated by excitons and electron-hole pairs, with emission spanning over a large band depending on the 2D material [90]. Cryogenic measurements also revealed the presence of trions (excitons bound to a carrier) and localized excitons. The latter are excitons trapped in a potential well created by atomic defects or impurities in the crystal lattice of the TMDCs. Similar to quantum dots (QDs), defect-bound excitons can behave like SPEs with smaller energy with respect to excitons due to the binding energy used to pin to disorder site. Quantum emission in TMDCs has been reported for both exfoliated [23, 91, 92] and grown WSe$_2$ [24].

For exfoliated materials, single photon emission is observed in localized sites along the interface between layers, the cracks or the edges of the flakes. In flakes grown by physical vapor transport [24], quantum emission is observed also in the center of the flake, suggesting a higher density of impurities and defects for artificially grown monolayers compared to the exfoliated ones.

Nevertheless, both systems show similar characteristics. A single localized exciton shows a rather narrow spectral emission with a linewidth down to 10 μeV with resonant excitation [93]. The lifetime has been measured to range from 600 ps up to 3 ns, depending on the investigated emitters. Blinking and spectral diffusion have been reported and still remain a big challenge for quantum emission applications with 2D materials. These issues can be solved by better isolating the monolayers (i.e. by encapsulation with hBN) from external agents that are responsible of fluctuation of the electronic environment surrounding these thin materials. Furthermore, quantum emitters have been shown to be rather resistant to high power excitation and several temperature cycles.

Single photon emission has also been investigated under strong electric and magnetic fields. Anomalously large Zeeman effect has been reported [23, 92], suggesting that the valley polarization degree of freedom, typical of hexagonal lattice structure, is preserved in the localized excitons. Several experimental works report a *g*-factor around 10, which is almost an order of magnitude larger than the one reported for III–V semiconductor QDs [94]. These observations strongly suggest that the quantum emitters in WSe_2 inherit their electronic structure from the TMDC and indicate trapped excitons as candidates.

Single photon emission can also be controlled and modulated via electrostatic gating [91]. In particular, the activity of the emitters is affected by the variation of the local electrical environment via gating. Emission stability is highly affected and deteriorated with increased bias. Preliminary measurements also showed that lifetime could also be controlled by external gating.

4.2 Single photon source in BN defect center

hBN is a vdW insulator widely used in heterostructures to improve optical and electronic properties of 2D semimetals and semiconductors [27]. Growing interest has been attracted also by its highly non-linear natural hyperbolic properties [95]. The recent demonstration of quantum emission in layered hBN opened the door to new applications in quantum technology as scalable single photon sources [96].

Different from TMDCs, where SPEs are associated to localized excitons, SPE in insulating hBN are attributed to atomic-like defects of the crystal structure, similar to color centers in diamond. Defects in hBN confine electronic levels within the band gap (~ 6 eV) and result in stable and extremely robust emitters.

Despite the wide use as insulator for its high quality, pristine hBN is not free of impurities, defects, and dangling bonds. Several luminescence experiments have reported strong emission from a large variety of charge defects, impurities, and adatoms [97–99] that create photoactive states within the hBN band gap [100, 101]. Recent studies demonstrate that these defects can be associated to nitrogen vacancies (NVs), a carbon atom substituted to an N vacancy or oxygen impurities [100]. Moreover, Tran et al. have shown that NVs in hBN function as SPEs [96]. Figure 6A shows the typical atomic structure of hBN with an individual atomic defect. The spectrally resolved emission of atomic defect at room temperature is shown in Figure 6B with the zero phonon line (ZPL) located around 575 nm and separated by ~ 50 nm from the first phonon side band.

Spectroscopy of SPEs is done in confocal configuration with a microscope objective of NA = 1 and a fiber-coupled spectrometer. In detection, the excitation laser at 532 nm is filtered out with a polarized beam splitter and long pass filter. Second-order correlation measurement shows good anti-bunching, unveiling the single photon nature of these emitters. An example is reported in Figure 6C where the coincidence counts are recorded using a Hanbury Brown and Twiss setup with continuous wave excitation. At zero delay time, the counts go below 0.5 ($g^2(0) = 0.24$), confirming the single photon emission. Power-dependent measurements revealed a three-level system with a metastable state. Moreover, these emitters are found to be stable over time and show high emission rate up to 4 million counts per second [102]. Time-dependent measurements indicate a lifetime around 2 ns.

Interestingly, experiments report different spectral shape for quantum emitters in hBN with the ZPL energy spanning over a large band, from the UV up to 750 nm [96, 103]. Figure 6D shows the spectral distribution of the ZPL emission energy of almost 90 emitters in our experiments.

Although individual emitters show different spectral shapes, the constant energy separation between the ZPL and the phonon side bands of ~ 160 meV suggests similar crystal structures [96]. It is also interesting to notice the correlation between the energy of the ZPL and the spectral shape. Recent studies suggest the presence of at least two families of quantum emitters in hBN with different lifetime and brightness [22].

An interesting aspect is the spectral distribution among the same family of emitter. Within the same family, the ZPL can span over the 300-meV band. The cause of this large distribution has been tentatively attributed to local strain fluctuations of the hBN flakes. Electronic disorder is induced in monolayer graphene by random strain
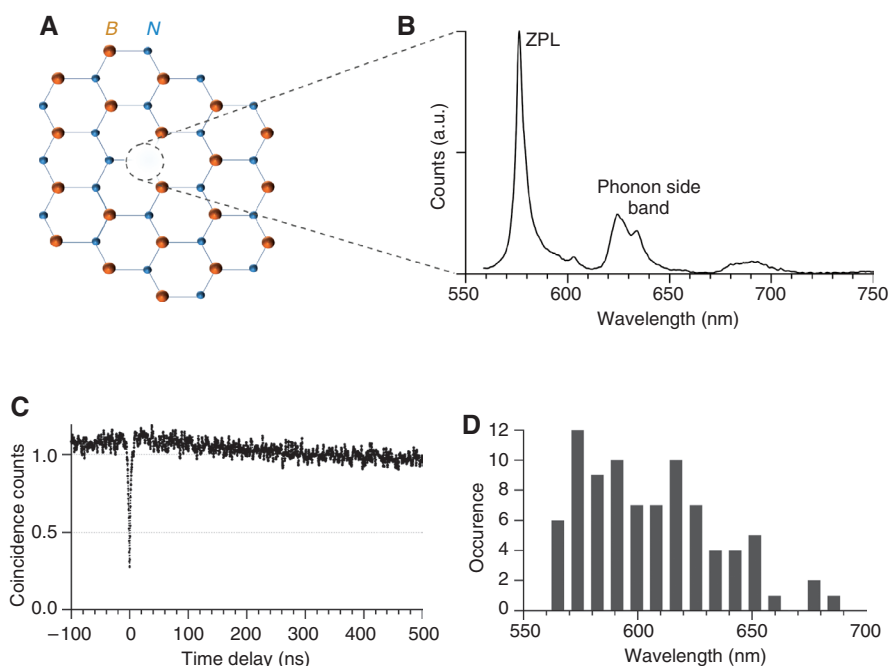
Figure 6: (A) Schematic of the atomic structure of hexagonal boron nitride. The dashed circle shows the structure of an NV in which one N atom is vacant and an adjacent B atom is substituted with N. (B) Typical room temperature spectrum of an SPE associated to an atomic-like defect. (C) Autocorrelation function ($g^2(\tau)$) showing anti-bunching at zero time delay. The histogram is measured using a Hanbury Brown and Twiss setup with continuous wave excitation at 532 nm. (D) Spectral distribution of the ZPL emission for almost 90 individual emitters. The emission energy spans over the 150-nm range.

fluctuation due to the exfoliation process or the inhomogeneous adhesion to the substrate [104]. Similarly, in hBN, strain can result in the displacement of the lattice atoms and the shifting of the energy levels of atomic-like defects. It has been calculated that strain in the range of − 5% to 5% can cause an energy shift of almost 200 meV, in agreement with the experimental observation.

The role of strain in the energy of the single photon emission can open interesting possibilities for the local tuning of the ZPL with applications in quantum computing and quantum information where indistinguishability is of utmost importance.

5 Outlook

Heterogeneous integration of 2D materials with nanophotonics promises a new architecture of optoelectronic devices and quantum photonics. In addition to E-O modulators and photodetectors based on graphene, a variety of combinations of 2D materials including TMDCs [90], BP [7, 17, 105], hBN, and superconducting 2D niobium diselenide (NbSe$_2$) [106] could further provide on-chip devices including all-optical modulators [107], mode-locked ultrafast laser [108], thermo-optic modulators [109], light-emitting diodes [110], and single photon sources [22].

Continued improvement in material and device fabrication is needed to facilitate the technology transition into applications. There has been significant progress in epitaxial, large-scale, and high-yield transfer processes for certain materials including graphene [14, 111, 112] and MoS$_2$ [113, 114]; on the other hand, the development of large-scale epitaxial hBN [115, 116] and other TMDCs continually advances. These developments could soon provide a hybrid platform that heterogeneously integrates 2D materials with silicon CMOS technology. To further ensure high-quality electronics and photonics based on 2D materials, suitable substrates and surface passivation are essential to ensure high-quality 2D devices. In addition, high-quality electrical contacts are also important to reduce contact resistance, improving device speed and power consumption. One-dimensional contacts to the hBN-encapsulated graphene [45] and graphite-graphene contacts [117] show great promise. Work continues on scaling up these processes and extending low-resistivity contacts to other 2D materials.

The outstanding optical and electronic properties of 2D materials offer a level of control, heterogeneous material properties, and design flexibilities that are probably unprecedented in optoelectronics. Here, we reviewed a subset of applications: optical interconnect

technologies including high-speed photodetectors [15, 16, 39] and modulators [10, 13], as well as device concepts for photonic quantum information processing, including progress toward efficient single photon sources and single photon detectors. With the exceptional progress of the past decade, such a scalable 2D nanophotonic architecture could bring remarkable impacts for these applications in the near future, while promising other directions including back-end deposited silicon photonics [118], mid-infrared photonics [119], THz detection [120, 121] and modulation [122], and also flexible photonics [123].

References

[1] Miller DAB. Device requirements for optical interconnects to silicon chips. Proc IEEE 2009;97:1166–85.

[2] Bergman K, Carloni LP, Biberman A, Chan J, Hendry G. Photonic Network-on-Chip Design. Springer, New York, 2014.

[3] Hochberg M, Baehr-Jones T. Towards fabless silicon photonics. Nat Photonics 2010;4:492–4.

[4] Liu K. Review and perspective on ultrafast wavelength-size electro-optic modulators. Laser Photonics Rev 2015;9:172–94.

[5] Heck MJR, Bauters JF, Davenport ML, et al. Hybrid silicon photonic integrated circuit technology. IEEE J Sel Top Quant Electron 2013;19:6100117.

[6] Liu Y, Ran Ye C, Khan S, Sorger VJ. Van der Waals heterostructures and devices. Nat Rev Mater 2016;1:16042.

[7] Xia F, Wang H, Xiao D, Dubey M, Ramasubramaniam A. Two-dimensional material nanophotonics. Nat Photonics 2014;8:899–907.

[8] Liu M, Yin X, Ulin-Avila E, et al. A graphene-based broadband optical modulator. Nature 2011;474:64–7.

[9] Liu M, Yin X, Zhang X. Double-layer graphene optical modulator. Nano Lett 2012;12:1482–5.

[10] Gao Y, Shiue RJ, Gan X, et al. High-speed electro-optic modulator integrated with graphene-boron nitride heterostructure and photonic crystal nanocavity. Nano Lett 2015;15:2001–5.

[11] Qiu C, Gao W, Vajtai R, et al. Efficient modulation of 1.55 μm radiation with gated graphene on a silicon microring resonator. Nano Lett 2014;14:6811–5.

[12] Ding Y, Zhu X, Xiao S, et al. Effective electro-optical modulation with high extinction ratio by a graphene-silicon microring resonator. Nano Lett 2015;15:4393–400.

[13] Phare CT, Daniel Lee Y-H, Cardenas J, Lipson M. Graphene electro-optic modulator with 30 GHz bandwidth. Nat Photonics 2015;9:511–4.

[14] Schall D, Neumaier D, Mohsin M, et al. 50 GBit/s photodetectors based on wafer-scale graphene for integrated silicon photonic communication systems. ACS Photonics 2014;1:781–4.

[15] Shiue RJ, Gao Y, Wang Y, et al. High-responsivity graphene-boron nitride photodetector and autocorrelator in a silicon photonic integrated circuit. Nano Lett 2015;15:7288–93.

[16] Gan X, Shiue R-J, Gao Y, et al. Chip-integrated ultrafast graphene photodetector with high responsivity. Nat Photonics 2013;7:883–7.

[17] Youngblood N, Chen C, Koester SJ, Li M. Waveguide-integrated black phosphorus photodetector with high responsivity and low dark current. Nat Photonics 2015;9:247–52.

[18] Gan X, Gao Y, Mak KF, et al. Controlling the spontaneous emission rate of monolayer MoS_2 in a photonic crystal nanocavity. Appl Phys Lett 2013;103:181119.

[19] Wu S, Buckley S, Schaibley JR, et al. Monolayer semiconductor nanocavity lasers with ultralow thresholds. Nature 2015;520:69–72.

[20] Ye Y, Wong ZJ, Lu X, et al. Monolayer excitonic laser. Nat Photonics 2015;9:733–7.

[21] Fong KC, Schwab KC. Ultrasensitive and wide-bandwidth thermal measurements of graphene at low temperatures. Phys Rev X 2012;2:031006.

[22] Tran TT, Elbadawi C, Totonjian D, et al. Robust multicolor single photon emission from point defects in hexagonal boron nitride. ACS Nano 2016;10:7331–8.

[23] Koperski M, Nogajewski K, Arora A, et al. Single photon emitters in exfoliated WSe_2 structures. Nat Nanotechnol 2015;10:503–6.

[24] He YM, Clark G, Schaibley JR, et al. Single quantum emitters in monolayer semiconductors. Nat Nanotechnol 2015;10:497–502.

[25] Gan X, Mak KF, Gao Y, et al. Strong enhancement of light-matter interaction in graphene coupled to a photonic crystal nanocavity. Nano Lett 2012;12:5626.

[26] Gan X, Shiue RJ, Gao Y, et al. Controlled light-matter interaction in graphene electrooptic devices using nanophotonic cavities and waveguides. IEEE J Sel Top Quant Electron 2014;20:95–105.

[27] Dean CR, Young AF, Meric I, et al. Boron nitride substrates for high-quality graphene electronics. Nat Nanotechnol 2010;5:722–6.

[28] Mak KF, Sfeir MY, Wu Y, et al. Measurement of the optical conductivity of graphene. Phys Rev Lett 2008;101:196405.

[29] Kravets VG, Grigorenko AN, Nair RR, et al. Spectroscopic ellipsometry of graphene and an exciton-shifted van Hove peak in absorption. Phys Rev B Condens Matter Mater Phys 2010;81:155413.

[30] Wu S, Buckley S, Jones A, et al. Control of two-dimensional excitonic light emission via photonic crystal. 2D Mater 2014;1:011001.

[31] Splendiani A, Sun L, Zhang Y, et al. Emerging photoluminescence in monolayer MoS_2. Nano Lett 2010;10:1271–5.

[32] Mak KF, Lee C, Hone J, et al. Atomically thin MoS_2: a new direct-gap semiconductor. Phys Rev Lett 2010;105:136805.

[33] Schwagmann A, Kalliakos S, Ellis D, et al. In-plane single-photon emission from a L3 cavity coupled to a photonic crystal waveguide. Opt Express 2012;20:28614.

[34] Chalcraft A, Lam S, O'Brien D, et al. Mode structure of the L3 photonic crystal cavity. Appl Phys Lett 2007;90:241117.

[35] Salehzadeh O, Djavid M, Tran NH, Shih I, Mi Z. Optically pumped two-dimensional MoS_2 lasers operating at room-temperature. Nano Lett 2015;15:5302–6.

[36] Liu X, Galfsky T, Sun Z, et al. Strong light–matter coupling in two-dimensional atomic crystals. Nat. Photonics 2014;9:30–4.

[37] Li H, Anugrah Y, Koester SJ, Li M. Optical absorption in graphene integrated on silicon waveguides. Appl Phys Lett 2012;101:2–7.

[38] Lu Z, Zhao W. Nanoscale electro-optic modulators based on graphene-slot waveguides. J Opt Soc Am B 2012;29:1490.

[39] Wang J, Cheng Z, Chen Z, et al. High-responsivity graphene-on-silicon slot waveguide photodetectors. Nanoscale 2016;8:13206–11.

[40] Wang F, Zhang Y, Tian C, et al. Gate-variable optical transitions in graphene. Science 2008;320:206–9.

[41] Li ZQ, Henriksen EA, Jiang Z, et al. Dirac charge dynamics in graphene by infrared spectroscopy. Nat Phys 2008;4:532–5.

[42] Mohsin M, Schall D, Otto M, et al. Graphene based low insertion loss electro-absorption modulator on SOI waveguide. Opt Express 2014;22:15292.

[43] Gan X, Shiue R-J, Gao Y, et al. High-contrast electrooptic modulation of a photonic crystal nanocavity by electrical gating of graphene. Nano Lett 2013;13:691–6.

[44] Dasgupta S, Stoesser G, Schweikert N, et al. Printed and electrochemically gated, high-mobility, inorganic oxide nanoparticle FETs and their suitability for high-frequency applications. Adv Funct Mater 2012;22:4909–19.

[45] Wang L, Meric I, Huang PY, et al. One-dimensional electrical contact to a two-dimensional material. Science 2013;342:614–7.

[46] Lee GHH, Yu Y-J, Lee C, et al. Electron tunneling through atomically flat and ultrathin hexagonal boron nitride. Appl Phys Lett 2011;99:1–4.

[47] Voskoboynikov VV, Gritsenko VA, Efimov VM, Lesnikovskaya VE, Edelman FL. Structure and electrophysical properties of boron nitride thin films. Phys Status Solidi 1976;34:85–94.

[48] Manipatruni S, Dokania RK, Schmidt B, et al. Wide temperature range operation of micrometer-scale silicon electro-optic modulators. Opt Lett 2008;33:2185–7.

[49] Teng J, Dumon P, Bogaerts W, et al. Athermal silicon-on-insulator ring resonators by overlaying a polymer cladding on narrowed waveguides. Opt Express 2009;17:14627–33.

[50] Reed GT, Mashanovich G, Gardes FY, Thomson DJ. Silicon optical modulators. Nat Photonics 2010;4:518–26.

[51] Youngblood N, Anugrah Y, Ma R, Koester SJ, Li M. Multifunctional graphene optical modulator and photodetector integrated on silicon waveguides. Nano Lett 2014;14:2741–6.

[52] Wang J, Lee S. Ge-photodetectors for Si-based optoelectronic integration. Sensors 2011;11:696–718.

[53] Liang D, Roelkens G, Baets R, Bowers JE. Hybrid integrated platforms for silicon photonics. Materials 2010;3:1782–1802.

[54] Atabaki AH, Meng H, Alloatti L, Mehta KK, Ram RJ. High-speed polysilicon CMOS photodetector for telecom and datacom. Appl Phys Lett 2016;109:111106.

[55] Mueller T, Xia F, Avouris P. Graphene photodetectors for high-speed optical communications. Nat Photonics 2010;4:297–301.

[56] Freitag M, Freitag M, Low T, Xia F, Avouris P. Photoconductivity of biased graphene. Nat Photonics 2012;7:53–9.

[57] Brida D, Tomadin A, Manzoni C, et al. Ultrafast collinear scattering and carrier multiplication in graphene. Nat Commun 2013;4:1987.

[58] Tielrooij KJ, Song JCW, Jensen SA, et al. Photoexcitation cascade and multiple hot-carrier generation in graphene. Nat Phys 2013;9:248–52.

[59] Özyilmaz B, Jarillo-Herrero P, Efetov D, Abanin DA, Levitov LS, Kim P. Electronic transport and quantum hall effect in bipolar graphene p-n-p junctions. Phys Rev Lett 2007;99:166804.

[60] Özyilmaz B, Jarillo-Herrero P, Efetov D, et al. Electronic transport in locally gated graphene nanoconstrictions. Appl. Phys. Lett. 2007;91:192107.

[61] Pospischil A, Humer M, Furchi MM, et al. CMOS-compatible graphene photodetector covering all optical communication bands. Nat Photonics 2013;7:892–6.

[62] Lu C, Fu Q, Huang S, Liu J. Polymer electrolyte-gated carbon nanotube field-effect transistor. Nano Lett 2004;4:623–7.

[63] Efetov DK, Maher P, Glinskis S, Kim P. Multiband transport in bilayer graphene at high carrier densities. Phys Rev B Condens Matter 2011;84:161412.

[64] Efetov DK, Kim P. Controlling electron-phonon interactions in graphene at ultrahigh carrier densities. Phys Rev Lett 2010;105:256805.

[65] Guo Y, Smith RB, Yu Z, et al. Li intercalation into graphite: direct optical imaging and Cahn-Hilliard reaction dynamics. J Phys Chem Lett 2016;7:2151–6.

[66] Song JCW, Rudner MS, Marcus CM, Levitov LS. Hot carrier transport and photocurrent response in graphene. Nano Lett 2011;11:4688–92.

[67] Gabor NM, Song JCW, Ma Q, et al. Hot carrier-assisted intrinsic photoresponse in graphene. Science 2011;334:648–52.

[68] Wang X, Cheng Z, Xu K, Tsang HK, Xu J-B. High-responsivity graphene/silicon-heterostructure waveguide photodetectors. Nat Photonics 2013;7:888–91.

[69] Guo Q, Pospischil A, Bhuiyan M, et al. Black phosphorus mid-infrared photodetectors with high gain. Nano Lett 2016;16:4648–55.

[70] Graham MW, Shi S-F, Ralph DC, Park J, McEuen PL. Photocurrent measurements of supercollision cooling in graphene. Nat Phys 2012;9:103–8.

[71] Liang T, Tsang H, Day I, et al. Silicon waveguide two-photon absorption detector at 1.5 μm wavelength for autocorrelation measurements. Appl Phys Lett 2002;81:1323.

[72] Hayat A, Nevet A, Ginzburg P, et al. Applications of two-photon processes in semiconductor photonic devices: invited review. Semicond Sci Technol 2011;26:083001.

[73] Duchesne D, Razzari L, Halloran L, et al. Two-photon detection in a MQW GaAs Laser at 1.55 μm. In: Conference on Lasers and Electro-Optics/International Quantum Electronics Conference, p. IMH5, OSA, Washington, DC, 2009.

[74] Tielrooij KJ, Piatkowski L, Massicotte M, et al. Generation of photovoltage in graphene on a femtosecond timescale through efficient carrier heating. Nat Nanotechnol 2015;10:437–43.

[75] Balandin AA. Thermal properties of graphene and nanostructured carbon materials. Nat Mater 2011;10:569–81.

[76] Balandin AA, Ghosh S, Bao W, et al. Superior thermal conductivity of single-layer graphene. Nano Lett 2008;8:902–7.

[77] Fong KC, Schwab KC. Publisher's note: ultrasensitive and wide-bandwidth thermal measurements of graphene at low temperatures. Phys Rev X 2012;2:031006.

[78] Fong KC, Wollman EE, Ravi H, et al. Measurement of the electronic thermal conductance channels and heat capacity of graphene at low temperature. Phys Rev X 2013;3:041008.

[79] Zuev YM, Chang W, Kim P. Thermoelectric and magnetothermoelectric transport measurements of graphene. Phys Rev Lett 2009;102:096807.

[80] McKitterick CB, Prober DE, Karasik BS. Performance of graphene thermal photon detectors. J Appl Phys 2013;113:044512.

[81] Wei J, Olaya D, Karasik BS, Pereverzev SV, Sergeev AV, Gershenson ME. Ultrasensitive hot-electron nanobolometers for terahertz astrophysics. Nat Nanotechnol 2008;3:496–500.

[82] Yan J, Kim M-H, Elle JA, et al. Dual-gated bilayer graphene hot-electron bolometer. Nat Nanotechnol 2012;7:472–8.

[83] Karasik BS, Pereverzev SV, Soibel A, et al. Energy-resolved detection of single infrared photons with $\lambda = 8\ \mu m$ using a superconducting microbolometer. Appl Phys Lett 2012;101:052601.

[84] Crossno J, Shi JK, Wang K, et al. Observation of the Dirac fluid and the breakdown of the Wiedemann-Franz law in graphene. Science 2016;351:1058–61.

[85] Efetov DK, Wang L, Handschin C, et al. Specular interband Andreev reflections at van der Waals interfaces between graphene and $NbSe_2$. Nat Phys 2015;12:328–32.

[86] Wan Z, Kazakov A, Manfra M, et al. Induced superconductivity in high-mobility two-dimensional electron gas in gallium arsenide heterostructures. Nat. Commun. 2015;6:7426.

[87] Efetov DK, Efetov KB. Crossover from retro to specular Andreev reflections in bilayer graphene. Phys Rev B Condens Matter 2016;94:075403.

[88] Kimble HJ. The quantum internet. Nature 2008;453:1023–30.

[89] Knill E, Laflamme R, Milburn GJ. A scheme for efficient quantum computation with linear optics. Nature 2001;409:4652.

[90] Mak KF, Shan J. Photonics and optoelectronics of 2D semiconductor transition metal dichalcogenides. Nat Photonics 2016;10:216–26.

[91] Chakraborty C, Kinnischtzke L, Goodfellow KM, Beams R, Vamivakas AN. Voltage-controlled quantum light from an atomically thin semiconductor. Nat Nanotechnol 2015;10:507–11.

[92] Srivastava A, Sidler M, Allain AV, Lembke DS, Kis A, Imamoğlu A. Optically active quantum dots in monolayer WSe_2. Nat Nanotechnol 2015;10:491–6.

[93] Kumar S, Brotóns-Gisbert M, Al-Khuzheyri R, et al. Resonant laser spectroscopy of localized excitons in monolayer WSe_2. Optica 2016;3:882–6.

[94] Bayer M, Ortner G, Stern O, et al. Fine structure of neutral and charged excitons in self-assembled In(Ga)As/(Al)GaAs quantum dots. Phys Rev B Condens Matter 2002;65:195315.

[95] Caldwell JD, Kretinin AV, Chen Y, et al. Sub-diffractional volume-confined polaritons in the natural hyperbolic material hexagonal boron nitride. Nat Commun 2014;5:5221.

[96] Tran TT, Bray K, Ford MJ, Toth M, Aharonovich I. Quantum emission from hexagonal boron nitride monolayers. Nat Nanotechnol 2015;11:37–41.

[97] Zunger A, Katzir A. Point defects in hexagonal boron nitride: II. Theoretical studies. Phys Rev B Condens Matter 1975;11:2378–90.

[98] Andrei EY, Katzir A, Suss JT. Point defects in hexagonal boron nitride: III. EPR in electron-irradiated BN. Phys Rev B Condens Matter 1976;13:2831–4.

[99] Garcia AGF, Neumann M, Amet F, et al. Effective cleaning of hexagonal boron nitride for graphene devices. Nano Lett 2012;12:4449–54.

[100] Wong D, Velasco J. Jr, Ju L, et al. Characterization and manipulation of individual defects in insulating hexagonal boron nitride using scanning tunnelling microscopy. Nat Nanotechnol 2015;10:949–53.

[101] Remes Z, Nesladek M, Haenen K, Watanabe K, Taniguchi T. The optical absorption and photoconductivity spectra of hexagonal boron nitride single crystals. Phys Stat Sol A 2005;202:2229–33.

[102] Martínez LJ, Pelini T, Waselowski V, et al. Efficient single photon emission from a high-purity hexagonal boron nitride crystal. Phys Rev B Condens Matter 2016;94:121405.

[103] Bourrellier R, Meuret S, Tararan A, et al. Bright UV single photon emission at point defects in h-BN. Nano Lett 2016;16:4317–21.

[104] Couto NJG, Costanzo D, Engels S. Random strain fluctuations as dominant disorder source for high-quality on-substrate graphene devices. Phys Rev X 2014;4:041019.

[105] Li L, Yu Y, Ye GJ, et al. Black phosphorus field-effect transistors. Nat Nanotechnol 2014;9:372–7.

[106] Ugeda MM, Bradley AJ, Zhang Y, et al. Characterization of collective ground states in single-layer $NbSe_2$. Nat Phys 2015;12:92–7.

[107] Li W, Chen B, Meng C, et al. Ultrafast all-optical graphene modulator. Nano Lett 2014;14:955–9.

[108] Sun Z, Hasan T, Torrisi F, et al. Graphene mode-locked ultrafast laser. ACS Nano 2010;4:803–10.

[109] Gan S, Cheng C, Zhan Y, et al. A highly efficient thermo-optic microring modulator assisted by graphene. Nanoscale 2015;4:163–4.

[110] Withers F, Del Pozo-Zamudio O, Mishchenko A, et al. Light-emitting diodes by band-structure engineering in van der Waals heterostructures. Nat Mater 2015;14:301–6.

[111] Lin Y-M, Valdes-Garcia A, Han S-J, et al. Wafer-scale graphene integrated circuit. Science 2011;332:1294–7.

[112] Gao L, Ni G-X, Liu Y, Liu B, Castro Neto AH, Loh KP. Face-to-face transfer of wafer-scale graphene films. Nature 2013;505:190–4.

[113] Wang H, Yu L, Lee Y-H, et al. Integrated circuits based on bilayer MoS_2 transistors. Nano Lett 2012;12:4674–80.

[114] Yu L, Lee YH, Ling X, et al. Graphene/MoS_2 hybrid technology for large-scale two-dimensional electronics. Nano Lett 2014;14:3055–63.

[115] Kim SM, Hsu A, Park MH, et al. Synthesis of large-area multi-layer hexagonal boron nitride for high material performance. Nat Commun 2015;6:8662.

[116] Jang A-R, Hong S, Hyun C, et al. Wafer-scale and wrinkle-free epitaxial growth of single-orientated multilayer hexagonal boron nitride on sapphire. Nano Lett 2016;16:3360–6.

[117] Chari T, Ribeiro-Palau R, Dean CR, Shepard K. Resistivity of rotated graphite-graphene contacts. Nano Lett 2016;16:4477–82.

[118] Lee YHD, Lipson M. Back-end deposited silicon photonics for monolithic integration on CMOS. IEEE J Sel Top Quantum Electron 2013;19:8200207.

[119] Shankar R, Leijssen R, Bulu I, Lončar M. Mid-infrared photonic crystal cavities in silicon. Opt Express 2011;19:5579.

[120] Vicarelli L, Vitiello MS, Coquillat D, et al. Graphene field-effect transistors as room-temperature terahertz detectors. Nat Mater 2012;11:865–71.

[121] Cai X, Sushkov AB, Suess RJ, et al. Sensitive room-temperature terahertz detection via the photothermoelectric effect in graphene. Nat Nanotechnol 2014;9:814–9.

[122] Gao W, Shu J, Reichel K, et al. High-contrast terahertz wave modulation by gated graphene enhanced by extraordinary transmission through ring apertures. Nano Lett 2014;14:1242–8.

[123] Li L, Lin H, Qiao S, et al. Integrated flexible chalcogenide glass photonic devices. Nat Photonics 2014;8:643–9.